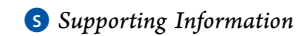
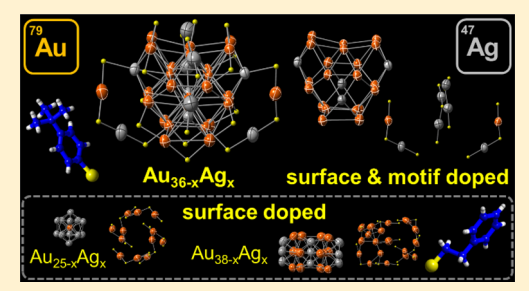
# Crystal Structure of Au<sub>36-x</sub>Ag<sub>x</sub>(SPh-tBu)<sub>24</sub> Nanoalloy and the Role of Ag Doping in Excited State Coupling

Naga Arjun Sakthivel, † Mauro Stener, Luca Sementa, Marco Medves, Guda Ramakrishna, Alessandro Fortunelli, Allen G. Oliver, and Amala Dass\*, on the control of the co

<sup>&</sup>lt;sup>1</sup>Dipartimento di Scienze Chimiche e Farmaceutiche, Università di Trieste, Trieste I-34127, Italy



**ABSTRACT:** We report the X-ray crystal structure of  $Au_{36-x}Ag_x(SPh-tBu)_{24}$ alloy nanomolecules, optical properties, and the substitutional disorder refinement protocol to obtain a reliable structural model. Single crystal X-ray crystallography (SC-XRD) revealed a composition of Au<sub>33,17</sub>Ag<sub>2,83</sub>(SPhtBu)<sub>24</sub> with 2 Ag doped on the 28-atom face centered cubic core surface and 0.83 Ag distributed over metal atoms on dimeric staple motifs. Electrospray ionization mass spectrometry revealed a composition of Au<sub>32.5</sub>Ag<sub>3.5</sub>(SPhtBu)<sub>24</sub> complementing the SC-XRD data. Optical properties were investigated by steady-state and transient absorption spectroscopies and computational studies, showing faster excited-state decay for Ag-doped



clusters due to enhanced electronic coupling. A previously published SC-XRD based Au<sub>36-x</sub>Ag<sub>x</sub>(SPh-tBu)<sub>24</sub> structure used positional disorder refinement and concluded that the structure is "solely motif-doped". But the structure has unusually large and small thermal ellipsoids indicating potential problems with the atom assignment. Here, we have modeled our SC-XRD data using both positional disorder and substitutional disorder. Subtitutional disorder modeling gave better R<sub>1</sub> and other refinement indicators, and similarly sized thermal ellipsoids. The resulting substitutional disorder model structure has Ag atoms not as "solely motif-doped" but is found both in the staple motifs and in the core. The substitutional disorder refinement for alloy nanomolecules must be performed at each metal site with independent free variables to determine the partial occupancy of hetero atoms. The positional disorder refinement should be performed for atoms or groups disordered over different positions typically found in disordered *t*Bu group ligands.

#### ■ INTRODUCTION

Alloy nanomolecules (NM) exhibit new or enhanced properties compared to that of the parent compound. 1-6 Alloying or doping of a heterometal atom compound can be achieved by co-reduction of different metal salts and thiolate ligand mixture, by reacting a homometallic NMs with a heterometal salt, and by reacting nanomolecules of different metals.<sup>6-12</sup> Other types of ligands such as alkynyl, selenophenol, and triphenylphosphines are also being employed as protecting groups instead of thiolate ligands. <sup>13–16</sup> Each of these methods have opened new avenues for making nanoalloys with interesting properties. 5,7,8,17-20

A wide array of Au and Ag based alloy nanomolecules have been reported and several have also been crystallographically studied. <sup>9,21–27</sup> Single crystal X-ray crystallography (SC-XRD) of the alloy NMs is crucial because it enables us to understand how the properties are tuned by doping heteroatoms at the atomic level. 2,28-34 The structural model refinement of the homometallic NMs are straightforward. However, alloy NMs structural model must be performed by substitutional disorder refinement with individual free variables for each of the metal sites to achieve a reliable model.

Au<sub>36</sub> with 28 core Au atom with four interpenetrating cuboctahedra in a FCC arrangement is one of the stable nanomolecules and it has been prepared with different types of ligands: thiolates, selenolates, and alkynes. 14,35-41 Au<sub>36</sub> protected by TBBT can be synthesized in high yields and can be stored for several years. 42,43 Aromatic thiolate protected Au<sub>36</sub> NMs have two optical absorption bands ~370 nm and ~575 nm with an optical band gap of ~1.7 eV and an electrochemical gap of ~2 V. 39,44 It has been shown to be an electrocatalyst for oxygen reduction reaction with relatively low overpotential and a 4e<sup>-</sup> process yielding water. 45 Au<sub>36</sub> also reversibly interconverts to Au<sub>30</sub> upon ligand exchange with the tBuSH. 46 Au<sub>36</sub>(TBBT)<sub>24</sub> has been studied with Ag doping at various Au:Ag ratios and a unique evolution of absorption

Received: September 24, 2019 Revised: November 6, 2019 Published: November 22, 2019

Department of Chemistry and Biochemistry, University of Mississippi, Oxford, Mississippi 38677, United States

<sup>\*</sup>Department of Chemistry, University of Notre Dame, Notre Dame, Indiana 46556, United States

<sup>§</sup>CNR-ICCOM & IPCF, Consiglio Nazionale delle Ricerche, Pisa I-56124, Italy

Department of Chemistry, Western Michigan University, Kalamazoo, Michigan 49008, United States

enhancement with doping levels was observed.<sup>47</sup> Au<sub>36</sub> have so far been alloyed with Ag and Cu, but both of these crystal structures have not used individual free variables for substitutional disorder modeling, leading to mis-assignment of locations of heteroatoms (Ag/Cu), namely, the "solely motif-doped" (vide infra).<sup>48,49</sup> Au<sub>36</sub> with a different type of kernel cocapped by chloride and 4-*tert*-butylbenzyl thiolate ligands has been reported.<sup>50</sup>

Although the crystal structure models hold valuable and rich structure-bonding information to understand the properties of nanomolecules and their alloy counterparts, care must be taken in modeling the structure to provide a model which would best represent the experimental diffraction data. In particular, the substitutional disorder refinement of partial occupancies of alloys must be done correctly using individual free variables. In the literature, some alloy crystal structures have been incorrectly refined using positional disorder (special position) modeling with EXYZ and EADP cards, leading to misassignments, and specifically assignments of heteroatoms to locations, where there is none.

Here, we report the following: (1) X-ray crystal structure of Au<sub>36-x</sub>Ag<sub>x</sub>(TBBT)<sub>24</sub>, (2) mass spectrometric analysis of the nanoalloy to determine the Ag composition, (3) a detailed substitutional disorder refinement protocol for alloy NMs, and a comparison with previous crystal structure that incorrectly used positional disorder modeling, (4) optical properties, studied both in absorption and via (4a) electron dynamics and (4b) computational studies.

## **EXPERIMENTAL SECTION**

**Materials.** Hydrogen tetrachloroaurate(III) (HAuCl<sub>4</sub>· 3H<sub>2</sub>O; Alfa Aesar ACS grade), silver nitrate (AgNO<sub>3</sub>; Alfa Aesar ACS grade), sodium borohydride (NaBH<sub>4</sub>; Acros, 99%), 4-tert-butylbenzene thiol (TBBT; TCI America, >97%), cesium acetate (Acros, 99%), and anhydrous ethyl alcohol (Acros, 99.5%) were used as received. HPLC grade solvents methylene chloride (DCM), tetrahydrofuran (THF), toluene, methanol, and ethanol were purchased from Fisher Scientific. All materials were used as received.

**Synthesis.** The  $\operatorname{Au}_{36-x}\operatorname{Ag}_x(\operatorname{SPh-}t\operatorname{Bu})_{24}$  nanomolecule was synthesized in two steps, first a polydisperse crude mixture of  $(\operatorname{AuAg})_x(\operatorname{TBBT})_y$  was obtained and thermochemically etched to obtain the product containing  $\operatorname{Au}_{36-x}\operatorname{Ag}_x$  as a major product.

Step 1.  $HAuCl_4:3H_2O$  (50 mg) and  $AgNO_3$  (Au:Ag = 1:0.33) were dissolved in THF (10 mL) and stirred (1200 rpm) for 10–15 min. Subsequently, TBBT ligand (AuAg:HSR = 1:5) was added to the solution and stirred for 30 min. This reaction mixture was reduced with  $NaBH_4$  (AuAg:NaBH<sub>4</sub> = 1:10) dissolved in ice cold water (5 mL). The reaction was stopped after 5 min and the solvent removed under reduced pressure, yielding an oily crude product. The crude product was washed with excess water and methanol to remove the byproducts and excess thiols.

*Step 2.* The crude product was then thermochemically etched<sup>51</sup> with excess TBBT ligand at 65 °C for 2 d. The etched product was washed with excess methanol to remove the byproducts and excess thiols. Final extraction was from DCM or toluene.

**Crystallization.** The single crystals of  $Au_{36-x}Ag_x(SPhtBu)_{24}$  alloy nanomolecules were grown by dissolving 5 mg of the as obtained etched product in DCM (1.5 mL) and layered with ethanol (1 mL) at 4 °C for ~2 months. The block-like black single crystals were used for SC-XRD study.

**Crystal Structure.** Crystal structure for  $C_{240}H_{312}Ag_{2.83}$ - Au<sub>33.17</sub> $S_{24}$ ; formula weight 10805.42; orthorhombic; space group  $P2_12_12$ ; a=24.016(5) Å; b=28.775(6) Å; c=22.090(4) Å;  $\alpha=90^\circ$ ;  $\beta=90^\circ$ ;  $\gamma=90^\circ$ ; volume = 15 266(5) ų; Z=2;  $\rho_{\rm calc}=2.351$  g/cm³;  $\mu=16.246$  mm<sup>-1</sup>; F(000) = 9779.0; 2Θ range = 2.83° to 46.234°; 225984 reflections collected; 21503 unique (Rint = 0.0722); giving  $R_1=0.0331$ ,  $wR_2=0.0742$  for 21503 with [I > 2 $\sigma$ (I)] and  $R_1=0.0385$ ,  $wR_2=0.0768$  for all 225 984 data. Residual electron density (e-·Å-3) max/min: 3.14/-1.30.

SC-XRD data collection was performed at 273 K on a Bruker Apex II diffractometer with Mo K\$\alpha\$ (\$\lambda\$ = 0.71073 Å) radiation source. The reflections were indexed by using the APEX II program suite. Data were corrected for absorption effects with SADABS using multiscan methods. The structure was solved with SHELXT and subsequent structure refinements were performed with SHELXL using Olex2 program. All non C and H atoms were refined anisotropically and the H atoms were added as riding atoms.

Alloy Crystal Structure Substitutional Disorder **Refinement.** The structure solution from the experimental diffraction was obtained by assigning all the metal atoms as Au, i.e., a formula of  $C_{240}S_{24}Au_{36}$  was used. The solution was then refined by SHELXL<sup>54</sup> least-squares method. One by one, all metal atom sites are assigned individual free variables in two PART instructions for Au and Ag partial occupancy along with EXYZ and EADP cards and refined (Figure S1). For a two component substitutional disorder refinement, the site occupancy factor (sof) for each metal site has to be modified from 11.0000 to 21.0000 (in PART 1), -21.0000 (in PART 2), and 31.0000 (in PART 1), -31.0000 (in PART 2) and so forth for all the metal sites (Figure S1). Accordingly, the element symbol in atom name and positional number in the SFAC line to indicate atom type for PART 2 instruction should be modified (Figure S1). After several cycles of refinement, sites with ≥10% Ag occupancy are retained for partial occupancy and the remaining are reverted to Au only. Then, followed by the several cycles of refinement, sites with ≥10% Ag occupancy are retained for partial occupancy, and the remaining are reverted to Au only. After repeating this procedure, sites that possess significant Ag occupancies can be reliably modeled for the nanoalloy molecule. The detailed ellipsoidal models, anisotropic displacement parameter (ADP) values, and partial occupancies during the various steps of substitutional disorder refinement are shown in Figures S2-S5.

Transient Absorption Measurements. Femtosecond transient absorption measurements were carried out at the Center for Nanoscale Materials, Argonne National Laboratory on  $\mathrm{Au}_{36}$  and Ag-doped  $\mathrm{Au}_{36}$ . Briefly, a Spectra Physics Tsunami Ti:sapphire, 75 MHz oscillator was used to seed a 5 kHz Spectraphysics Spitfire Pro regenerative amplifier. 95% of the output from the amplifier is used to pump a TOPAS optical parametric amplifier, which is used to provide the pump beam in a Helios transient absorption setup (Ultrafast Systems Inc.). A pump beam of 370 nm was used for the measurements. The remaining 5% of the amplified output is focused onto a sapphire crystal to create a white light continuum that serves as the probe beam in our measurements (450 to 750 nm). The pump beam was depolarized and chopped at 2.5 kHz and both pump and probe beams were overlapped in the sample for magic angle transient measurements. Optical absorption measurements were carried out to monitor the stability of the clusters with laser excitation.

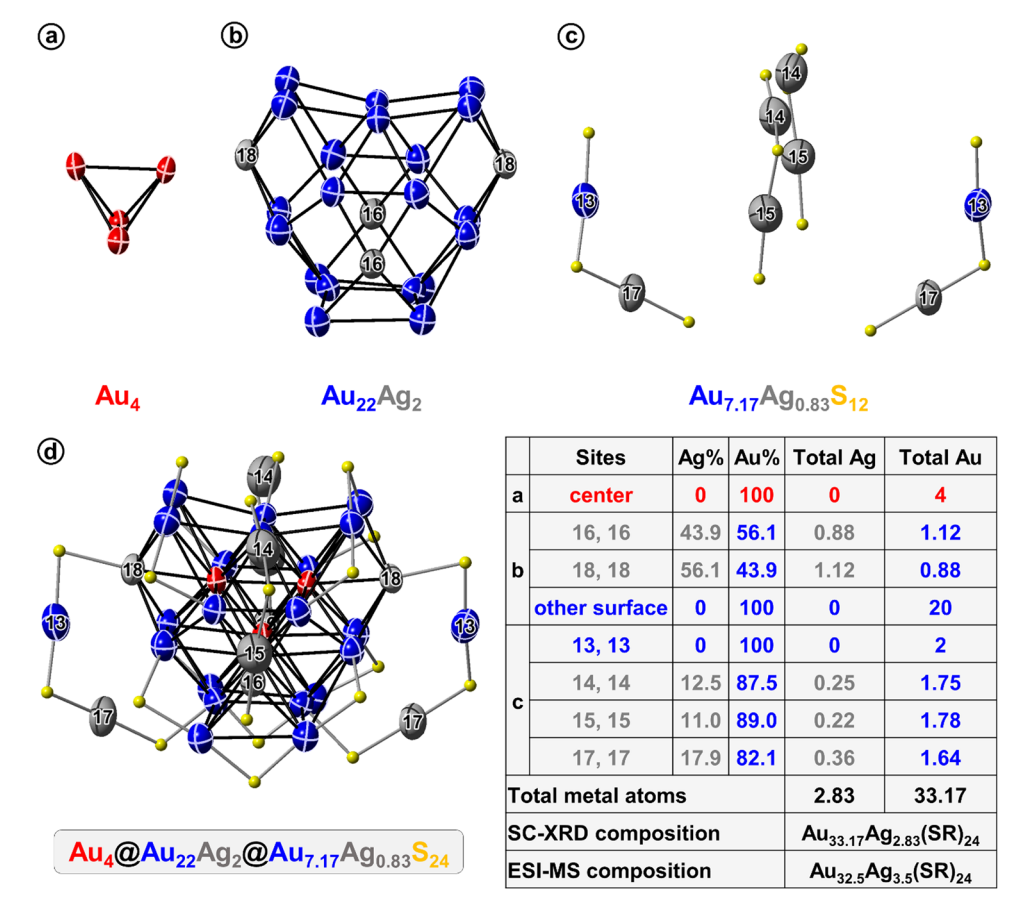


Figure 1. X-ray crystal structure of  $Au_{36-x}Ag_x(SPh-tBu)_{24}$  NMs. (a) 4 tetrahedral central Au atoms (red). (b) 24 metal atom sites following the central atoms, where 4 tetrahedrally symmetrical vertices sites are doped with Ag (16, 16, 18 and 18), contributing 2 Ag to the total composition. (blue, Au and gray, Ag partial occupancy sites) (c) 4 dimeric staples with 8 metal sites of which two metal sites (13, 13) has no Ag occupancy and rest of the sites contribute 7.17 Au and 0.83 Ag to the total composition. (d) 28 metal atom core protected by 4 dimeric staples and 12 bridging ligands. The anisotropic displacement parameter (ADP) is a key indicator to identify sites occupied by hetero metal atoms. Thermal ellipsoids' size and shape are visual indicators which reflects the ADP value and it is not revealed by typical ball and stick models. Therefore, metal sites are intentionally displayed as thermal ellipsoids to reveal the equally sized ellipsoids after modeling for substitutional disorder refinement (vide infra). Black bonds are bonds between metal atoms in core, gray bonds are S bonds to the metal sites. C and H groups of the ligand shell are excluded for clarity. Site-wise composition for the 36 metal sites is listed on the right-hand side table. SC-XRD and ESI-MS based (Au,Ag) composition are (33.17,2.83) and (32.5,3.5), respectively. The site numbers were assigned as in the crystallographic information file (CIF). Two sites have same site number (e.g., 16, 16) as the asymmetric unit in the crystal structure is half a molecule. Refer Figures S6 and S7 for ball and stick model view and the 24 surface atom site numbers, respectively. In the discussion below, some metal sites are described with a prime (') for clarity, they are symmetric sites generated from the asymmetric unit (for example, Ag16/Ag16').

**Instrumentation.** Electrospray Ionization mass spectrum (ESI-MS) was collected using a Waters Synapt HDMS instrument with THF as the solvent. Cesium acetate dissolved in anhydrous ethanol was used to facilitate the ionization. UV—vis absorption spectrum was collected using a Shimadzu UV-1601 spectrophotometer with toluene as the solvent.

## ■ RESULTS AND DISCUSSION

**Crystallography.** The  ${\rm Au_{36-x}Ag_x(SPh\text{-}}t{\rm Bu})_{24}$  NMs crystallized in an orthorhombic unit cell in the  $P2_12_12$  space group with 2 molecular units per unit cell. The final  ${\rm Au_{33.12}Ag_{2.88}(SPh\text{-}}t{\rm Bu})_{24}$  structural model has a  ${\rm R_1}$  value of 3.31%. The crystal structure of  ${\rm Au_{33.17}Ag_{2.83}}$  nanoalloy is presented in Figure 1. The structural framework of the  ${\rm Au_{33.17}Ag_{2.83}(SPh\text{-}}t{\rm Bu})_{24}}$  nanoalloy is identical to that of the parent compound  ${\rm Au_{36}(SR)_{24}}$ . This framework can be described in two different way; here we adopt the original description based on 28 metal atom FCC core protected by 12 bridging thiolate ligands ( $-{\rm Au\text{-}}S(R)\text{-}{\rm Au\text{-}}$ ) and 4 dimeric staple

motifs  $(-(R)S-Au-S(R)-Au-S(R)-)^{37,39}$  (for an alternative one see Theivendran et al. 47). The truncated tetrahedral 28 metal atom core is made up of 4 interpenetrating cuboctahedra consisting of 4 atom tetrahedron in the center and 24 atoms on the surface (Figure 1). On the core-surface, four dimeric staple motifs protect 8 metal atoms and the remaining 16 metal atoms are protected by 12 bridging ligands. In the Ag-doped Au<sub>36</sub>, the 4 sites on the surface of the core are heavily doped (~50%) by Ag while the remaining 20 surface atoms and 4 center atoms are Au only (Figure 1a and 1b). The four Ag atoms (Ag16, Ag16', Ag18, and Ag18', designated ExTd by Theivendran. 47) on the core-surface are doped in a tetrahedrally symmetrical fashion on the vertices of interpenetrating cuboctahedron protected by dimeric staple motifs (Figure 1b, only Ag containing sites are labeled for clarity, site numbers were assigned as in the crystallographic information file (CIF)). The partial occupancies at Ag16/Ag16' and Ag18/ Ag18' are 44% and 56%, respectively. These 4 heavily doped sites on the core contribute to 2 Ag in the overall composition (accounting for  $\sim$ 71% of Ag in the overall composition). The

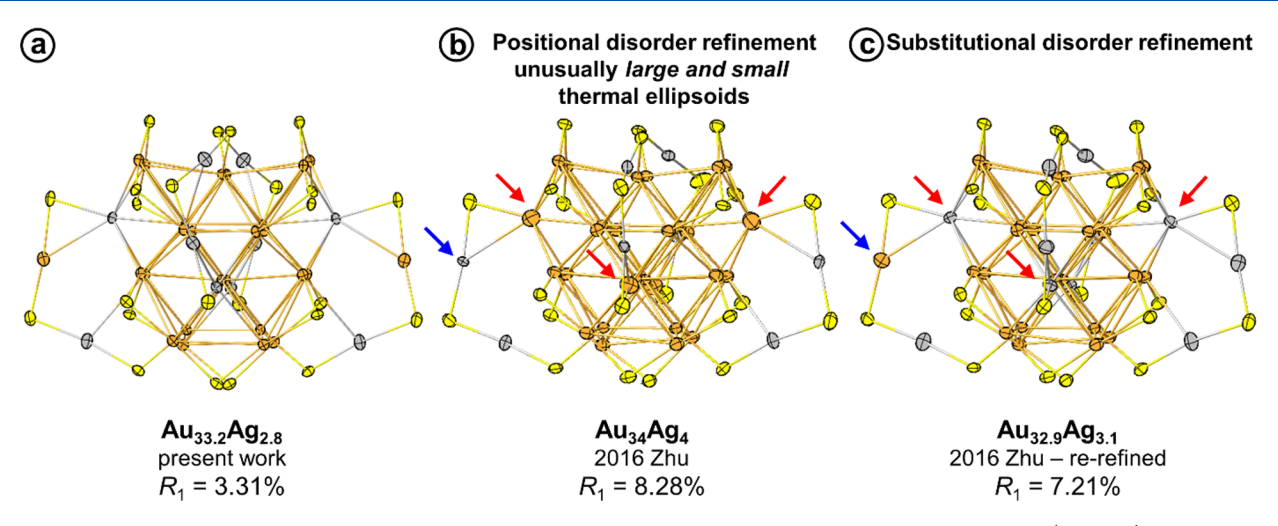


Figure 2. Comparison of X-ray crystal structure models refined for substitutional disorder by Ag doping in  $Au_{36}(SPh-tBu)_{24}$  nanomolecules.  $Au_{36-x}Ag_x(SPh-tBu)_{24}$  alloy structure model (a) from this present work, (b) from 2016 report with one free variable fixing 50% occupancy for 8 metal atom sites on dimeric staple motifs, and (c) structural model from 2016 report re-refined with independent free variables for each metal sites. Three of the thermal ellipsoids in (b) are indicated by red arrows revealing relatively higher ADP value than other Au atoms and in (c) ADP for the same site drops upon refinement for Ag partial occupancy leading to  $\sim$ 40–50% Ag occupancy on those sites. Blue arrow in (b) indicates a staple motif metal site (shrunk) with low ADP value whereas after refining for substitutional disorder, in (c) that site has only Au and the thermal ellipsoid is of similar size as neighboring sites. Totally in frame 2c, there are four Ag occupancy sites on the 28 atom FCC core surface, same as the structure obtained in the present work (Figure 1). Refer to the Experimental Section and Figures S2–S5 for detailed explanation on the substitutional disorder refinement. The work by Zhu et al. 48 is referred to as 2016 Zhu in (b) and (c).

remaining 0.83 Ag is spread out on the 6 dimeric staple motif sites (Ag14/Ag14', named ExSt-Near and Ag15/Ag15' and Ag17/Ag17', named ExSt-Far in Theivendran et al.<sup>47</sup>) with partial occupancies of 12.5%, 11%, and 18%, respectively (Figure 1C). The remaining two dimeric staple sites (Au13/Au13') are exclusively Au only (Figure 1C). Clearly, the level of Ag doping here achieved is smaller than that investigated previously,<sup>47</sup> so that we do not observe here phenomena such as the nonmonotonic behavior of optical properties as a function of doping content, as reported in our previous work.

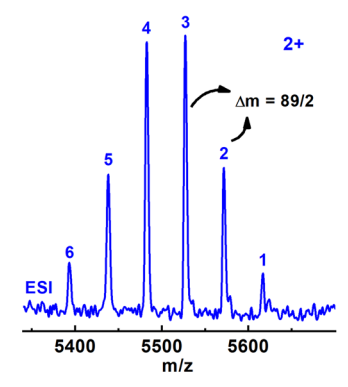
In the case of phenylethanethiolate protected  $Au_{25-x}Ag_x$  and  $Au_{38-x}Ag_{xx}$ . Au atoms were doped exclusively on the core surface. In the case of aromatic TBBT ligand protected  $Au_{36-x}Ag_{xx}$ , it was reported that the Ag atoms are exclusively doped on the 8 Au atoms in dimeric staple motifs with 50% Ag occupancy at each of those sites (using positional disorder) contributing to 4 Ag atoms in the overall composition. However, here we show that better modeling with improved  $R_1$  values is obtained allowing for partial Ag occupancy by refining for substitutional disorder, leading to a significant population of the core surface sites (Figure 2), similar to the results discussed in Figure 1. This directly contradicts with the "solely motif-doped" conclusion from the earlier report. This finding is more consistent with computational results indicating that Ag doping on the core surface is energetically preferred.

Substitutional Disorder vs Positional Disorder Refinement of Au<sub>36-x</sub>Ag<sub>x</sub>. One of the key indicators for substitutional disorder in metal sites is the presence of *large or small atomic displacement parameter (ADP) values* compared to other sites which are occupied by only one element. The ADP values of the sites occupied with multiple elements, vary significantly after refining for substitutional disorder with individual free variables (Figure 2) and is reflected in the size of the ellipsoids. Figure 2 shows the comparison between ellipsoidal models for SC-XRD data from this work, 2016 report 48 and 2016 model re-refined following the protocol

described above (detailed protocol is provided in the Experimental Section).

The erroneous use of positional disorder modeling (instead of substitutional disorder modeling) resulted in the conclusion that the Ag atoms are "solely motif-doped". For the 2016 Zhu paper, we extracted the data from the published crystallographic information file (CIF) embedded with hkl data, we hypothesized that the small and large thermal ellipsoids arise from substitutional disorder. We modeled it for substitutional disorder (instead of positional disorder as in 2016 Zhu paper) and the resulting model after refinement resulted in equally sized thermal ellipsoids and improved  $R_1$  values. The Ag occupancy sites and percentage Ag partial occupancies in the re-refined model of 2016 Zhu paper (Figures 2b, S4, and S5) are very similar to the findings in this work (Figures 1, 2a, S2, and S3).

To describe this in crystallographic terminology, Figure 2b was modeled by using positional disorder modeling for Au/Ag partial occupancy of the 8 staple motif metal sites with a special position, site occupancy factor (sof) of 10.5000 for Au and Ag sites in PART instructions coupled with EXYZ and EADP cards. (EXYZ assigns same x, y and z parameters to the named atoms, for example, EXYZ Au18 Ag18, instructs two elements to occupy the same position (coordinates). EADP assigns same isotropic or anisotropic displacement parameters for the named atoms.) This led to fixed 50% Ag occupancy on staple motifs metal sites and unusually large and small thermal ellipsoid sizes, as indicated by the red and blue arrows in Figure 2b, respectively. The sof value of 10.5000 for an atom in an ordered structure conveys that the site is at a special position located on a 2-fold axis or on an inversion center.<sup>57</sup> In the 2016 report, using the special position sof for substitutional disorder refinement lead to the "solely motif-doped" structure with 50% Ag occupancy on staple metal sites. In Figure 2c, after substitutional disorder modeling (Figures S4 and S5), the thermal ellipsoids were equally sized and Ag occupancy sites are similar to Figure 2a result from our work. We also refined



_		ESI-MS
nanomolecules	%Ag as total	Ag contribution from each species
$Au_{35}Ag_1(SR)_{24}$	4.76	0.05
$Au_{34}Ag_2(SR)_{24}$	15.8	0.32
$Au_{33}Ag_3(SR)_{24}$	29.6	0.89
$Au_{32}Ag_4(SR)_{24}$	28.9	1.16
$Au_{31}Ag_5(SR)_{24}$	15.0	0.75
$Au_{30}Ag_6(SR)_{24}$	5.86	0.35
total Ag		3.51

Figure 3. ESI mass spectra of  $Au_{36-x}Ag_x(SPh-tBu)_{24}$  alloy NMs with x=1-6.  $Au_{36-x}Ag_x(SPh-tBu)_{24}Cs_2^{2+}$  peaks of the alloy NMs. Each peak has a m/z difference of 89/2 Da corresponding to the 2+ charge state and mass difference between Au and Ag. The total Ag contributed to overall composition based on mass spectrometry is determined based on the peak intensity and are listed in the table.

our SC-XRD data similar to 2016 Zhu paper instead of substitutional disorder to illustrate how that affects the structure model (Figure S8). The staple motif metal sites were modeled for 50% partial occupancy by positional disorder refinement. It led to an increase in R<sub>1</sub> value from 3.31% to 4.73%, unusually large and small thermal ellipsoids, and site 13 which has no significant Ag occupancy showed a non-positive definite.

In the Au<sub>36-x</sub>Cu<sub>x</sub> structure report, the model has several metal sites linked by only two free variables for Au/Cu partial occupancy with sof values of 21.0000,-21.0000 (4 sites) and 31.0000,-31.0000 (10 sites) instead of 14 independent free variables. 49 This led to a Cu partial occupancy of 21.5% and 13.3% in 4 sites and 10 sites, respectively (Figure S8).<sup>49</sup> Figure S9 reveals the unusually elongated thermal ellipsoids on 4 staple motif sites with 21.5% Cu occupancy linked by one free variable, instead of four independent free variables.

Mass Spectrometry. The composition of  $Au_{36-x}Ag_x(SPh$ tBu)<sub>24</sub> alloy NMs was determined by ESI-MS to independently verify the composition determined by SC-XRD.  $Au_{36-x}Ag_x(SR)_{24}$  alloy NMs ionized in its +2 charge state with two Cs+ adducts facilitating the ionization of the neutral compound. The m/z peaks were observed at 5617, 5572, 5527, 5482, 5438, and 5393 Da with a difference of ~45 Da corresponding to half the mass difference between an Au and Ag atom (89 Da/2; Figure 3). The Ag<sub>x</sub> ranges from 1 to 6 and the average Ag contribution to the total composition was determined by considering the peak intensities, yielding an average composition of Au<sub>32,49</sub>Ag<sub>3,51</sub>(SPh-tBu)<sub>24</sub> (Figure 3). The relative contribution from each Au<sub>36-x</sub>Ag<sub>x</sub>(SR)<sub>24</sub> species (Au<sub>35</sub>Ag<sub>1</sub>, Au<sub>34</sub>Ag<sub>2</sub>, Au<sub>33</sub>Ag<sub>3</sub>, Au<sub>32</sub>Ag<sub>4</sub>, Au<sub>31</sub>Ag<sub>5</sub>, and Au<sub>30</sub>Ag<sub>6</sub>) are 4.96, 15.8, 29.6, 28.9, 15.0, and 5.86%, respectively (Figure 3 table). The average Ag composition determined by mass spectrometry is in reasonable agreement with the crystallographically determined formula of Au<sub>33,17</sub>Ag<sub>2,83</sub>(SPh-tBu)<sub>24</sub>. The difference in AuAg composition between mass spectrometry and SC-XRD could stem from the fact that the crystallographic model accounts only for significant Ag partial occupancies (≥10%) over several cycles of refinement and/or difference in ionization efficiency. The SC-XRD re-refined model of the previous report 48 has a composition of Au<sub>32.88</sub>Ag<sub>3.12</sub>(SPh-tBu)<sub>24</sub> and it is also in close agreement with our results and similar site occupancies.

**Optical Studies.** The  $Au_{36-x}Ag_x(TBBT)_{24}$  alloy nanomolecule exhibits absorption features at ~373 and ~565 nm and a prominent shoulder at ~425 nm whereas the homometallic Au<sub>36</sub>(TBBT)<sub>24</sub> nanomolecule has two prominent absorption bands at ~376 nm and ~575 nm and a broad shoulder at ~412 nm (Figure 4). The 373 and 376 nm features

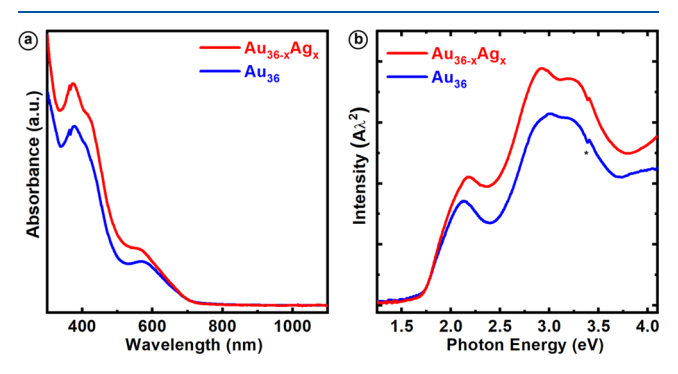


Figure 4. (a) UV-vis absorption spectra and (b) photon energy plot of Au<sub>36-x</sub>Ag<sub>x</sub>(SPh-tBu)<sub>24</sub> alloy compared with the parent compound  $Au_{36}(SPh-tBu)_{24}$ . red is  $Au_{36-x}Ag_x$  alloy and blue is  $Au_{36}$ . instrumental artifact.

are almost similar in both the systems whereas there is a red shift in the shoulder at ~412 to ~425 nm and a blue shift in the ~575 nm peak to ~565 nm. Apart from these details, one can observe that at this low level of Ag doping the overall appearance of the optical absorption spectra is similar for both pure Au and Ag-doped species. The optical band gap of the  $Au_{36-x}Ag_x(TBBT)_{24}$  alloy is not altered, and it is ~1.7 eV. The static optical response of the  $Au_{36-x}Ag_x(TBBT)_{24}$  alloy nanomolecule is similar to the previous report by Zhu et al. 48 This indicates that independent of the synthetic route the doping pattern and property of Au<sub>36</sub> system is constant. However, we will see that Ag doping brings about significant differences in the dynamical optical response of  $Au_{36-x}Ag_x(TBBT)_{24}$  alloy nanomolecules.

Transient Absorption Analysis. Metal doping of gold clusters can affect both ground and excited state optical properties. However, the optical absorption measurements of Au<sub>36</sub> and AgAu<sub>36</sub> reported above show no striking differences, suggesting that Ag-doping at this low level has little effect on the ground state optical properties. It is however still interesting to see the influence of Ag-doping on the excited state optical properties. Shown in Figure 5a are the excited state absorption (ESA) spectra at different time delays for Au<sub>36</sub> after excitation at 370 nm. Immediately after photoexcitation, a transient with a maxima around 480 and 660 nm is observed.

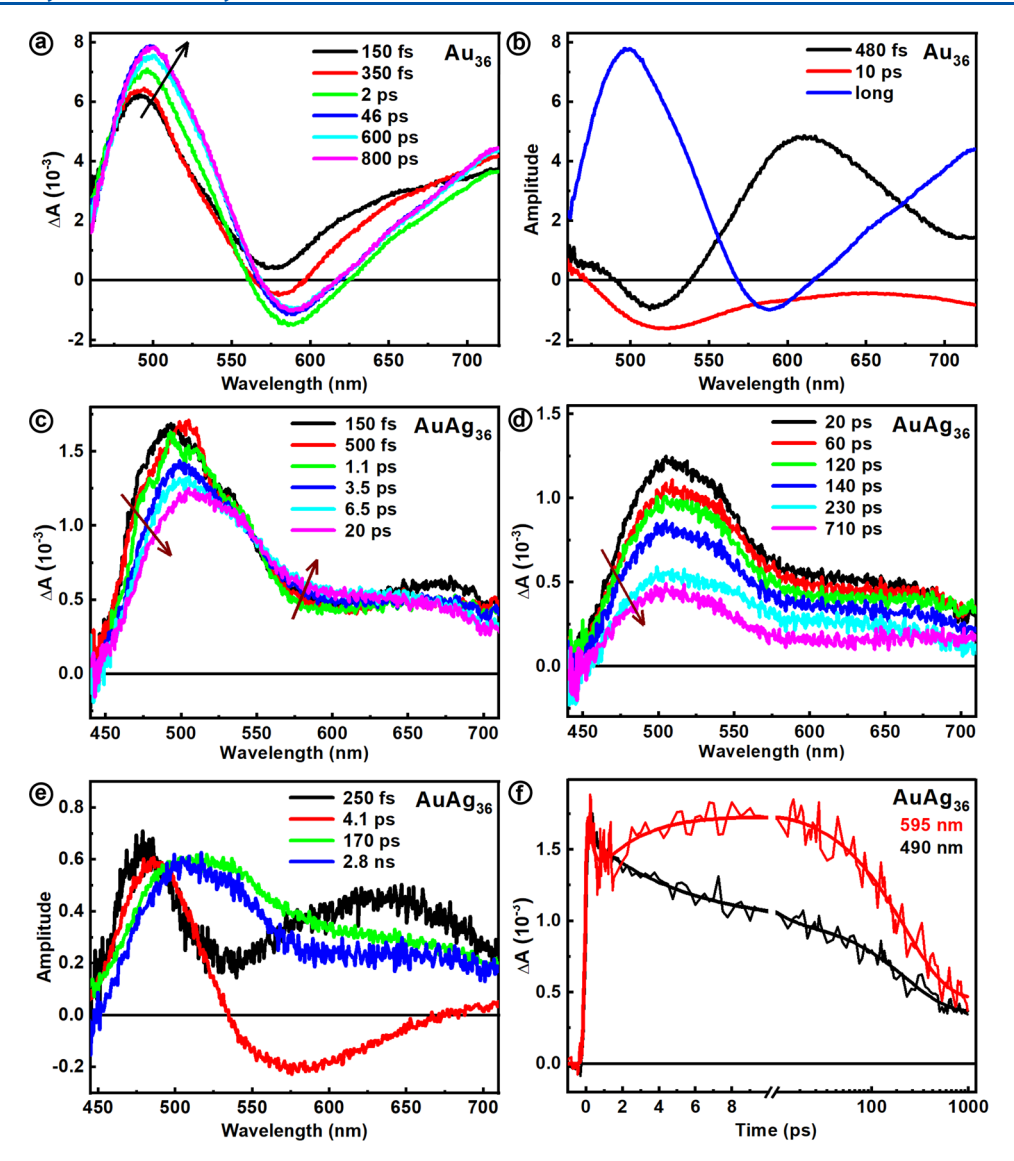


Figure 5. (a) Excited state absorption spectra at different time delays for  $Au_{36}$  and (b) species-associated spectra obtained from global fit analysis. Excited state absorption spectra at different time delays for  $Au_{36-x}Ag_x$  (noted as  $AuAg_{36}$ ) after excitation at 370 nm: (c) 150 fs to 20 ps and (d) 20 to 700 ps. (e) Species associated spectra obtained from global fit analysis. (f) Kinetic decay comparison at 490 nm (black) and 595 nm (red) showing the early relaxation and long-lived at two different wavelengths for  $AuAg_{36}$ .

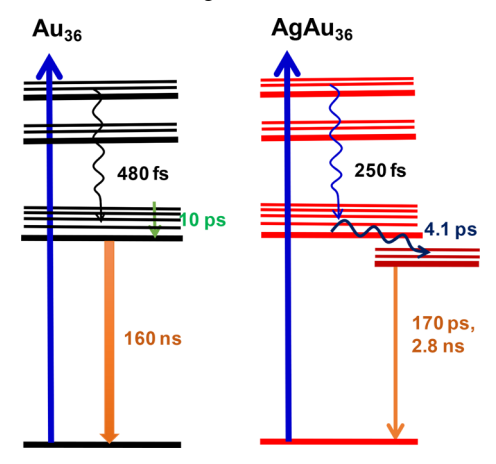
This transient grows and decays, giving rise to a bleach with a maximum around 570 nm. Species-associated spectra obtained from global fit analysis (Figure 5b) show three main components: the first one with a time scale of 480 fs, a second one with 10 ps and a long-lived transient. Subpicosecond relaxation of the 480 fs transient is assigned to intracore state relaxation, while the 10s of picosecond relaxation is related to the growth of the transient and is assigned to the thermalization that was observed only for Au<sub>36</sub> with aromatic ligands. The long-lived transient has a lifetime of 160 ns as determined from time-resolved luminescence measurements. The observed excited state relaxation is typical of most ligand-protected gold clusters. Let us now examine how the metal-doping altered the excited state relaxation dynamics.

Contrary to what is observed in steady-state measurements, the excited state absorption measurements show that Agdoping has a significant effect on the excited state relaxation dynamics. Shown in parts c and d of Figure 5 are the excited state absorption at short and long-time delays for AgAu<sub>36</sub> after

excitation at 370 nm. A decay of ESA from 150 fs to 20 ps at 490 nm followed by an increase between 550 to 630 nm is observed (Figure 5c). However, a consistent decay is observed at all wavelengths from 20 to 700 ps (Figure 5d) suggesting that the excited state relaxation became faster with Ag-doping with respect to pure Au<sub>36</sub>. For a better understanding, speciesassociated spectra were obtained from global fit analysis and are shown in Figure 5e. Interestingly, 4 components can be derived from this global fit analysis. The first component has a time scale of 250 fs that can be assigned to ultrafast intra-core state relaxation for AuAg<sub>36</sub>. It appears that the intra-core state relaxation becomes faster with Ag-doping. The 4.1 ps component spectral properties matched well with long-lived excited state of Au<sub>36</sub> indicating that the faster intra-core state relaxation populates the lowest excited state of Au<sub>36</sub> but that decays to give rise to another state which decays with 170 ps and 2.8 ns. A comparison of kinetic traces at 490 and 595 nm (Figure 5f) shows the 250 fs and 4.1 ps decay components followed by faster charge recombination back to ground state when compared to Au<sub>36</sub>. A comparison of long-lived states (Figure S10) of Au<sub>36</sub> and AuAg<sub>36</sub> shows that overall lifetime of Au<sub>36</sub> has decreased to around 2 ns from 160 ns of Au<sub>36</sub>.

Overall, the excited state relaxation of Ag-doped Au<sub>36</sub> can be summarized as shown in Scheme 1. Intra-core state relaxation

Scheme 1. Cartoon Diagram Depicting the Excited-State Relaxation in  $Au_{36}$  and  $AgAu_{36}$  Clusters



and thermalization followed by 160 ns decay with photoluminescence is observed for  $Au_{36}$ . Upon Ag-doping, the intracore state relaxation became faster ending with the lowest excited state of  $(AuAg)_{36}$  which decays to give rise to dark states with probable contributions from the shell-gold comprising of Ag. These shell-gold states decay nonradiatively with lifetimes of 170 ps and 2.8 ns, which are much faster than those observed in  $Au_{36}$ .

Theoretical Analysis of the Optical Response. The structural and static optical properties of Ag<sub>x</sub>Au<sub>36-x</sub>(TBBT)<sub>24</sub> nanomolecules were investigated using first-principles densityfunctional theory (DFT) and time-dependent DFT (TDDFT) modeling, along the lines of our previous work.<sup>47</sup> Within our computational method, we cannot achieve a statistical occupation of sites by Ag, therefore we have taken the experimental X-ray structure and produced a few isomers (homotops) by replacing selected Au atoms with Ag. In particular, in the following we will focus on two models with composition Ag<sub>4</sub>Au<sub>32</sub>(TBBT)<sub>24</sub>, in which we replaced either the [17,17',18,18'] Au atoms  $(Ag_4Au_{32}\text{-ExTd-ExStFar} \text{ in the}$ nomenclature of Theivendran et al. 47) or the [15,15',16,16'] Au atoms (Ag<sub>4</sub>Au<sub>32</sub>-ExTd-ExStNear in the nomenclature of Theivendran et al.<sup>47</sup>). The coordinates of the (Ag/Au,S) atoms were frozen to those of the Ag<sub>x</sub>Au<sub>36-x</sub>(TBBT)<sub>24</sub> crystallographic structure, while the organic part (CH atoms) were

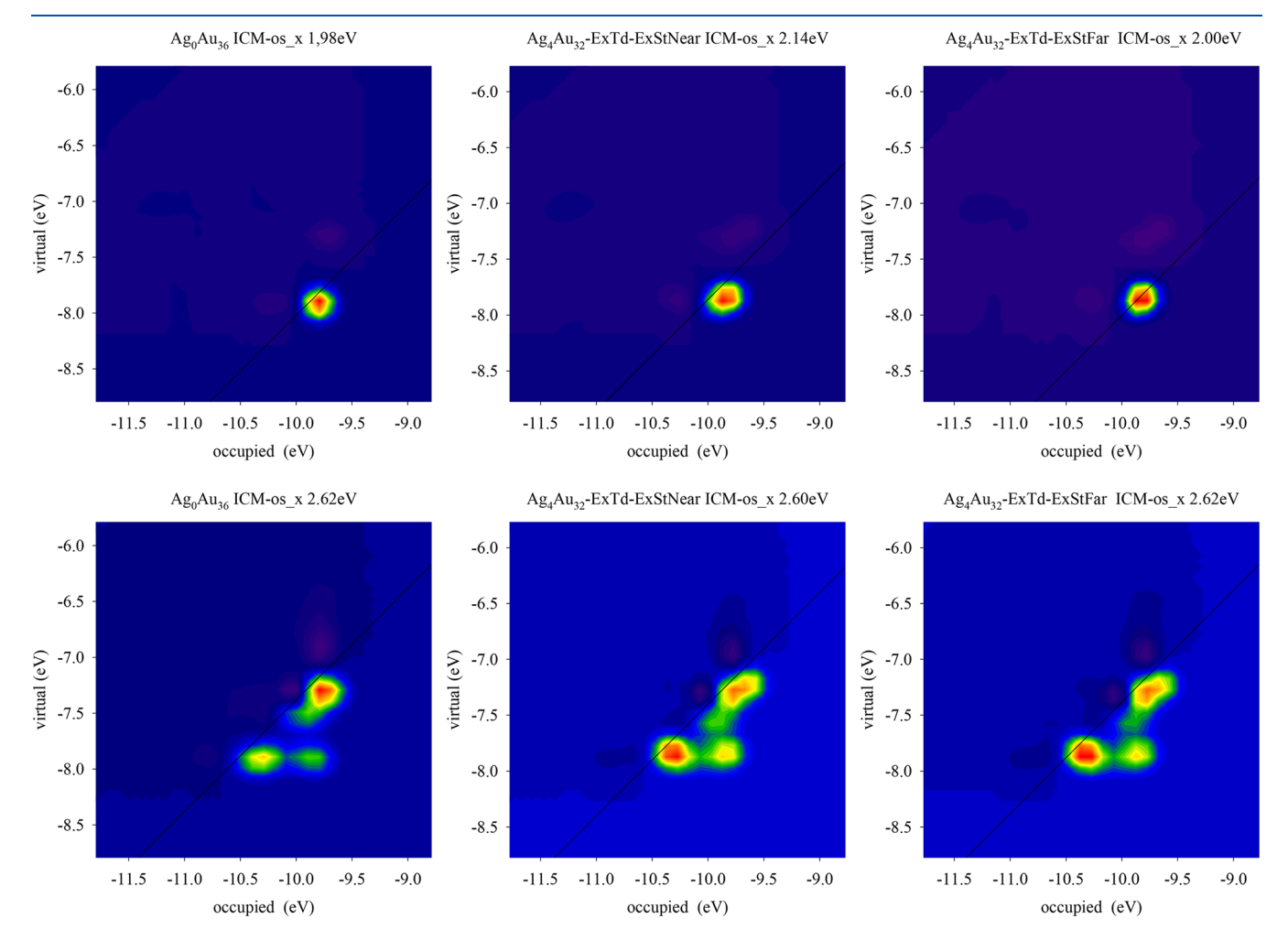


Figure 6. ICM-OS plots (x Cartesian component) for  $\mathrm{Au}_{36}(\mathrm{SPh}\text{-}t\mathrm{Bu})_{24}$  and the two homotop  $\mathrm{Ag}_4\mathrm{Au}_{32}(\mathrm{SPh}\text{-}t\mathrm{Bu})_{24}$  model clusters considered in this work in the energy region corresponding to the 580 nm (upper boxes) and 500 nm (lower boxes), see text for details.

relaxed at DFT level. DFT calculations were performed by employing the CP2K code<sup>58</sup> within the hybrid Gaussian/ Plane-Wave scheme (GPW). Core electrons were described with pseudopotentials derived by Goedecker, Teter, and Hutter<sup>59</sup> whereas DZVP basis sets<sup>60</sup> were used for representing the DFT Kohn-Sham valence orbitals. The cutoff for the auxiliary plane wave representation of the density was 400 Ry. Calculations were performed spin-unrestricted. The semiempirical Grimme-D3 correction<sup>61</sup> was added to Perdew-Burke-Ernzerhof (PBE)<sup>62</sup> exchange and correlation (xc-) functional to take into account dispersion interactions. It can be noted that the Ag<sub>4</sub>Au<sub>32</sub>-ExTd-ExStFar homotop is more stable than the Ag<sub>4</sub>Au<sub>32</sub>-ExTd-ExStNear homotop by 0.19 eV, in contrast with the findings of Theivendran et al., 47 Table S1, suggesting that the use of experimental geometries can tune the theoretical predictions, as previously observed. 65

On the so-derived geometries, optical spectra were simulated using TDDFT via a complex polarizability algorithm, 64,65 the ADF package,66 and the LB94 exchange-correlation potential,<sup>67</sup> while the exchange-correlation kernel in the TDDFT part was approximated according to the Adiabatic LDA (ALDA).<sup>68</sup> A STO basis set of TZP quality was employed, which has proven to provide accurate results.<sup>69</sup> The Zero Order Regular Approximation (ZORA)<sup>70</sup> was employed to include relativistic effects. The imaginary frequency employed to introduce finite lifetime of the excited state was fixed to 0.075 eV. Calculations were performed spin-restricted for predicting TDDFT response.

TDDFT/LB94 spectra were also analyzed in terms of Individual Component Maps of Oscillator Strength (ICM.-OS) plots, as proposed in Theivendran et al.<sup>47</sup> These plots visualize the contribution to the Oscillator Strength from single-particle excitations in the (virtual/occupied) molecular orbital plane for an excited state at a given energy and in a given Cartesian direction of the exciting electric field.

The calculated photoabsorption profiles of Au<sub>36</sub>(SPh-tBu)<sub>24</sub> and the two homotop Ag<sub>4</sub>Au<sub>32</sub>(SPh-tBu)<sub>24</sub> model nanomolecules are reported in Figures S11 and S12. A qualitatively similar profile was obtained for the pure and doped clusters in agreement with the experimental data. It is reasonable considering the low level of doping and the fact that most of Ag atoms occupy the ExTd sites which are energetically favorable (and should thus be preferably occupied when doping achieves thermodynamic equilibrium) but induce a smaller effect on optical absorption<sup>47</sup> (a more detailed discussion is provided in the SI). Although the absorption spectrum is not strongly affected by silver alloying, the transient absorption analysis has identified, for the silver doped clusters, two-state dynamics. This indicates that the decay mechanism passes through a higher exited state (at 500 nm) whose population constantly decreases, followed by a low-lying excited state (at 580 nm) whose population increases before eventually decaying to the ground state. To shed light on this mechanism however being unable to model long-time excitedstate dynamics, we investigated the nature of the excited states at the ICM-OS level, which corresponds to the experimental features at 500 and 580 nm. ICM-OS plots are reported in Figure 6. The nature of the low-lying excited state (upper panels) is similar for the pure gold clusters and the two alloy homotops containing 4 silver atoms: the presence of only one spot on the straight line corresponding to orbital energy differences equal to the excitation energy suggests a "molecular" behavior without coupling. In contrast, the nature

of the higher-energy excited state (lower panel) is more complex: two spots on the straight line are supplemented by a third spot which is off-diagonal and suggests a strong coupling with lower-energy configurations. The third off-line spot corresponds to the low-energy excited state, so that a coupling between higher- and lower-energy excited states is disclosed from this analysis. Even more interestingly, such off-diagonal spot is much more pronounced in the silver alloys than in the pure gold cluster, suggesting that such coupling is much more effective in the presence of silver. This helps rationalize the dynamics observed in the transient absorption experiment: while in pure gold cluster the decay to the ground state is direct, since there is weak coupling with the low-lying state, in silver alloys such coupling is stronger and the decay to this intermediate low-lying excited state is favored. To give a more complete description of the different excited states, in Figures S13, S14, and S15 of the SI we report plots of the molecular orbitals involved. These plots show that all occupied and virtual orbitals mostly contributing to the single-particles excitations here involved are localized on the cluster ligand shell and outer metal core, with strong S contribution as well as significant contributions from metal staple atoms and atoms on the cluster surface, while the contribution of the organic residues are smaller although not negligible. The present analysis demonstrates the usefulness of the ICM-OS analysis to reveal coupling between excited states. Finally, the ICM-OS plots in Figure 6 also reveal that the similar absorption intensity between pure and Ag-doped systems actually results from a compensation (negative interference) between singleparticle contributions giving rise to increasing and decreasing intensity: as discussed in Theivendran et al.,<sup>47</sup> absorption intensity corresponds to an absolute value and can therefore mask subtle quantum effects which are revealed in dynamics.

# CONCLUSIONS

In summary, the crystal structure of TBBT protected Au<sub>36-x</sub>Ag<sub>x</sub> nanomolecules has revealed that the core-centered metal sites are occupied by Au atoms only (Au<sub>4</sub>), Ag hetero atoms significantly populates 4 sites on the core-surface (Au<sub>22</sub>Ag<sub>2</sub>), and Ag occupies 10-20% on 6 metal sites in the dimeric staple motifs while 2 sites are occupied by Au only. The doping pattern observed here is more consistent with computational results indicating that Ag doping on the core surface is energetically preferred.<sup>47</sup> The composition of the Au<sub>36-x</sub>Ag<sub>x</sub> nanomolecules determined by mass spectrometry agrees reasonably well with the SC-XRD structure. The optical absorption spectrum of the nanoalloy has absorption features at  $\sim$ 373,  $\sim$  425, and  $\sim$ 565 nm. It is similar to the previous report by Zhu et al.<sup>48</sup> and the re-refined structural model of their data also exhibits a similar doping pattern as determined in this work. It indicates that care must be taken in performing the substitutional disorder refinement to obtain a reliable structural model.

We also studied the excited state optical properties of the Au<sub>36</sub> and Au<sub>36-x</sub>Ag<sub>x</sub> alloy nanomolecules and ICM-OS analyses to provide insights into the experimental results. Transient absorption studies revealed that, Ag doping leads to faster excited state decay lifetimes compared to the Au<sub>36</sub> nanomolecules. ICM-OS analyses revealed that Ag doping in Au<sub>36</sub> leads to a stronger coupling between higher- and lower-energy excited states complementing the results from transient absorption measurements.

#### ASSOCIATED CONTENT

# Supporting Information

The Supporting Information is available free of charge at https://pubs.acs.org/doi/10.1021/acs.jpcc.9b09060.

CCDC deposition number 1955713 (CIF)

Detailed figures, crystal structure tables, TDDFT details, transient decay kinetics, TDDFT spectra, molecular orbitals, substitutional disorder refinement (PDF)

# AUTHOR INFORMATION

## **Corresponding Author**

\*E-mail: amal@olemiss.edu.

**ORCID** ®

Naga Arjun Sakthivel: 0000-0001-8134-905X

Mauro Stener: 0000-0003-3700-7903 Guda Ramakrishna: 0000-0002-5288-8780 Alessandro Fortunelli: 0000-0001-5337-4450

Amala Dass: 0000-0001-6942-5451

**Notes** 

The authors declare no competing financial interest.

## ACKNOWLEDGMENTS

NSF-CHE-1808138 and NSF-CHE-1255519 supported the work performed by N.S. and A. D. We gratefully acknowledge the support by Vignesh Raja Ganesh Raj in SC-XRD data collection and 2019 American Crystallographic Association Summer course. G.R. acknowledges the support of Western Michigan University-FRACAA and Dr. Gary Wiederrecht, Argonne national laboratory for help with transient absorption measurements. Use of the Center for Nanoscale Materials, an Office of Science user facility, was supported by the U.S. Department of Energy, Office of Science, Office of Basic Energy Sciences, under Contract No. DE-AC02-06CH11357. A.F. and L.S. gratefully acknowledge the computational support at CINECA supercomputing center (ISCRA awards HP10B89V25 and HP10BSR1VZ).

# REFERENCES

- (1) Kumara, C.; Dass, A. AuAg)<sub>144</sub>(SR)<sub>60</sub> Alloy Nanomolecules. *Nanoscale* **2011**, *3*, 3064–3067.
- (2) Kumara, C.; Aikens, C. M.; Dass, A. X-ray Crystal Structure and Theoretical Analysis of  $Au_{25-x}Ag_x(SCH_2CH_2Ph)_{18}^-$  Alloy. *J. Phys. Chem. Lett.* **2014**, *5*, 461–466.
- (3) Kumara, C.; Zuo, X.; Cullen, D. A.; Dass, A. Au<sub>329-x</sub>Ag<sub>x</sub>(SR)<sub>84</sub> Nanomolecules: Plasmonic Alloy Faradaurate-329. *J. Phys. Chem. Lett.* **2015**, *6*, 3320–3326.
- (4) Kumara, C.; Gagnon, K. J.; Dass, A. X-ray Crystal Structure of Au<sub>38-x</sub>Ag<sub>x</sub>(SCH<sub>2</sub>CH<sub>2</sub>Ph)<sub>24</sub> Alloy Nanomolecules. *J. Phys. Chem. Lett.* **2015**, *6*, 1223–1228.
- (5) Kwak, K.; Choi, W.; Tang, Q.; Kim, M.; Lee, Y.; Jiang, D.-e.; Lee, D. A Molecule-like  $PtAu_{24}(SC_6H_{13})_{18}$  Nanocluster as an Electrocatalyst for Hydrogen Production. *Nat. Commun.* **2017**, *8*, 14723.
- (6) Hossain, S.; Ono, T.; Yoshioka, M.; Hu, G.; Hosoi, M.; Chen, Z.; Nair, L. V.; Niihori, Y.; Kurashige, W.; Jiang, D.-e.; et al. Thiolate-Protected Trimetallic Au<sub>~20</sub>Ag<sub>~4</sub>Pd and Au<sub>~20</sub>Ag<sub>~4</sub>Pt Alloy Clusters with Controlled Chemical Composition and Metal Positions. *J. Phys. Chem. Lett.* **2018**, *9*, 2590–2594.
- (7) Hossain, S.; Niihori, Y.; Nair, L. V.; Kumar, B.; Kurashige, W.; Negishi, Y. Alloy Clusters: Precise Synthesis and Mixing Effects. *Acc. Chem. Res.* **2018**, *51*, 3114–3124.
- (8) Wang, S.; Li, Q.; Kang, X.; Zhu, M. Customizing the Structure, Composition, and Properties of Alloy Nanoclusters by Metal Exchange. *Acc. Chem. Res.* **2018**, *51*, 2784–2792.

- (9) Yan, J.; Teo, B. K.; Zheng, N. Surface Chemistry of Atomically Precise Coinage—Metal Nanoclusters: From Structural Control to Surface Reactivity and Catalysis. *Acc. Chem. Res.* **2018**, *51*, 3084—3093
- (10) Gan, Z.; Xia, N.; Wu, Z. Discovery, Mechanism, and Application of Antigalvanic Reaction. *Acc. Chem. Res.* **2018**, *51*, 2774–2783.
- (11) Chakraborty, I.; Pradeep, T. Atomically Precise Clusters of Noble Metals: Emerging Link between Atoms and Nanoparticles. *Chem. Rev.* **2017**, *117*, 8208–8271.
- (12) Krishnadas, K. R.; Baksi, A.; Ghosh, A.; Natarajan, G.; Som, A.; Pradeep, T. Interparticle Reactions: An Emerging Direction in Nanomaterials Chemistry. *Acc. Chem. Res.* **2017**, *50*, 1988–1996.
- (13) Wang, Y.; Wan, X.-K.; Ren, L.; Su, H.; Li, G.; Malola, S.; Lin, S.; Tang, Z.; Häkkinen, H.; Teo, B. K.; et al. Atomically Precise Alkynyl-Protected Metal Nanoclusters as a Model Catalyst: Observation of Promoting Effect of Surface Ligands on Catalysis by Metal Nanoparticles. *J. Am. Chem. Soc.* **2016**, *138*, 3278–3281.
- (14) Rambukwella, M.; Chang, L.; Ravishanker, A.; Fortunelli, A.; Stener, M.; Dass, A. Au<sub>36</sub>(SePh)<sub>24</sub> Nanomolecules: Synthesis, Optical Spectroscopy and Theoretical Analysis. *Phys. Chem. Chem. Phys.* **2018**, 20, 13255–13262.
- (15) Bootharaju, M. S.; Chang, H.; Deng, G.; Malola, S.; Baek, W.; Häkkinen, H.; Zheng, N.; Hyeon, T. Cd<sub>12</sub>Ag<sub>32</sub>(SePh)<sub>36</sub>: Non-Noble Metal Doped Silver Nanoclusters. *J. Am. Chem. Soc.* **2019**, *141*, 8422–8425.
- (16) Shichibu, Y.; Negishi, Y.; Watanabe, T.; Chaki, N. K.; Kawaguchi, H.; Tsukuda, T. Biicosahedral Gold Clusters  $[Au_{25}(PPh_3)_{10}(SC_nH_{2n+1})SCl_2]^{2+}$  (n = 2–18): A Stepping Stone to Cluster-Assembled Materials. *J. Phys. Chem. C* **2007**, *111*, 7845–7847.
- (17) Jiang, D.-e.; Whetten, R. L. Magnetic Doping of a Thiolated-Gold Superatom: First-Principles Density Functional Theory Calculations. *Phys. Rev. B: Condens. Matter Mater. Phys.* **2009**, 80, 115402.
- (18) Choi, W.; Hu, G.; Kwak, K.; Kim, M.; Jiang, D.-e.; Choi, J.-P.; Lee, D. Effects of Metal-Doping on Hydrogen Evolution Reaction Catalyzed by MAu<sub>24</sub> and M<sub>2</sub>Au<sub>36</sub> Nanoclusters (M = Pt, Pd). ACS Appl. Mater. Interfaces **2018**, 10, 44645–44653.
- (19) Pelton, M.; Tang, Y.; Bakr, O. M.; Stellacci, F. Long-Lived Charge-Separated States in Ligand-Stabilized Silver Clusters. *J. Am. Chem. Soc.* **2012**, *134*, 11856–11859.
- (20) Soldan, G.; Aljuhani, M. A.; Bootharaju, M. S.; AbdulHalim, L. G.; Parida, M. R.; Emwas, A.-H.; Mohammed, O. F.; Bakr, O. M. Gold Doping of Silver Nanoclusters: A 26-Fold Enhancement in the Luminescence Quantum Yield. *Angew. Chem., Int. Ed.* **2016**, *55*, 5749–5753.
- (21) Desireddy, A.; Conn, B. E.; Guo, J.; Yoon, B.; Barnett, R. N.; Monahan, B. M.; Kirschbaum, K.; Griffith, W. P.; Whetten, R. L.; Landman, U.; et al. Ultrastable Silver Nanoparticles. *Nature* **2013**, 501, 399–402.
- (22) Yoon, B.; Luedtke, W. D.; Barnett, R. N.; Gao, J.; Desireddy, A.; Conn, B. E.; Bigioni, T.; Landman, U. Hydrogen-Bonded Structure and Mechanical Chiral Response of A Silver Nanoparticle Superlattice. *Nat. Mater.* **2014**, *13*, 807–811.
- (23) Yang, H.; Wang, Y.; Huang, H.; Gell, L.; Lehtovaara, L.; Malola, S.; Häkkinen, H.; Zheng, N. All-Thiol-Stabilized Ag<sub>44</sub> and Au<sub>12</sub>Ag<sub>32</sub> Nanoparticles with Single-Crystal Structures. *Nat. Commun.* **2013**, *4*, 2422.
- (24) Yang, H.; Wang, Y.; Edwards, A. J.; Yan, J.; Zheng, N. High-Yield Synthesis and Crystal Structure of A Green Au<sub>30</sub> Cluster Co-Capped by Thiolate and Sulfide. *Chem. Commun.* **2014**, *50*, 14325–14327.
- (25) Yang, H.; Wang, Y.; Chen, X.; Zhao, X.; Gu, L.; Huang, H.; Yan, J.; Xu, C.; Li, G.; Wu, J.; et al. Plasmonic Twinned Silver Nanoparticles with Molecular Precision. *Nat. Commun.* **2016**, *7*, 12800
- (26) Sels, A.; Salassa, G.; Pollitt, S.; Guglieri, C.; Rupprechter, G.; Barrabés, N.; Bürgi, T. Structural Investigation of the Ligand

- Exchange Reaction with Rigid Dithiol on Doped (Pt, Pd) Au<sub>25</sub> Clusters. J. Phys. Chem. C **2017**, 121, 10919–10926.
- (27) Kazan, R.; Zhang, B.; Bürgi, T. Au<sub>38</sub>Cu<sub>1</sub>(2-PET)<sub>24</sub> Nanocluster: Synthesis, Enantioseparation and Luminescence. *Dalton Trans* **2017**, 46, 7708–7713.
- (28) Weerawardene, K. L. D. M.; Häkkinen, H.; Aikens, C. M. Connections Between Theory and Experiment for Gold and Silver Nanoclusters. *Annu. Rev. Phys. Chem.* **2018**, *69*, 205–229.
- (29) Weerawardene, K. L. D. M.; Aikens, C. M. Origin of Photoluminescence of Ag<sub>25</sub>(SR)<sub>18</sub> Nanoparticles: Ligand and Doping Effect. *J. Phys. Chem. C* **2018**, *122*, 2440–2447.
- (30) Alkan, F.; Pandeya, P.; Aikens, C. M. Understanding the Effect of Doping on Energetics and Electronic Structure for Au<sub>25</sub>, Ag<sub>25</sub>, and Au<sub>38</sub> Clusters. *J. Phys. Chem. C* **2019**, *123*, 9516–9527.
- (31) Xu, W. W.; Zeng, X. C.; Gao, Y. Application of Electronic Counting Rules for Ligand-Protected Gold Nanoclusters. *Acc. Chem. Res.* **2018**, *51*, 2739–2747.
- (32) Conn, B. E.; Atnagulov, A.; Yoon, B.; Barnett, R. N.; Landman, U.; Bigioni, T. P. Confirmation of a De novo Structure Prediction for an Atomically Precise Monolayer-Coated Silver Nanoparticle. *Sci. Adv.* **2016**, *2*, No. e1601609.
- (33) Conn, B. E.; Atnagulov, A.; Bhattarai, B.; Yoon, B.; Landman, U.; Bigioni, T. P. Synthetic and Postsynthetic Chemistry of  $M_4Au_xAg_{44-x}(p-MBA)_{30}$  Alloy Nanoparticles. *J. Phys. Chem. C* **2018**, 122, 13166–13174.
- (34) Suyama, M.; Takano, S.; Nakamura, T.; Tsukuda, T. Stoichiometric Formation of Open-Shell  $[PtAu_{24}(SC_2H_4Ph)_{18}]^-$  via Spontaneous Electron Proportionation between  $[PtAu_{24}(SC_2H_4Ph)_{18}]^{2-}$  and  $[PtAu_{24}(SC_2H_4Ph)_{18}]^0$ . J. Am. Chem. Soc. 2019, 141, 14048–14051.
- (35) Price, R. C.; Whetten, R. L. All-Aromatic, Nanometer-Scale, Gold-Cluster Thiolate Complexes. J. Am. Chem. Soc. 2005, 127, 13750–13751.
- (36) Nimmala, P. R.; Dass, A. Au<sub>36</sub>(SPh)<sub>23</sub> Nanomolecules. *J. Am. Chem. Soc.* **2011**, *133*, 9175–9177.
- (37) Zeng, C.; Qian, H.; Li, T.; Li, G.; Rosi, N. L.; Yoon, B.; Barnett, R. N.; Whetten, R. L.; Landman, U.; Jin, R. Total Structure and Electronic Properties of the Gold Nanocrystal Au<sub>36</sub>(SR)<sub>24</sub>. Angew. Chem., Int. Ed. **2012**, 51, 13114–13118.
- (38) Das, A.; Liu, C.; Zeng, C.; Li, G.; Li, T.; Rosi, N. L.; Jin, R. Cyclopentanethiolato-Protected Au<sub>36</sub>(SC<sub>5</sub>H<sub>9</sub>)<sub>24</sub> Nanocluster: Crystal Structure and Implications for the Steric and Electronic Effects of Ligand. *J. Phys. Chem. A* **2014**, *118*, 8264–8269.
- (39) Nimmala, P. R.; Knoppe, S.; Jupally, V. R.; Delcamp, J. H.; Aikens, C. M.; Dass, A. Au<sub>36</sub>(SPh)<sub>24</sub> Nanomolecules: X-ray Crystal Structure, Optical Spectroscopy, Electrochemistry, and Theoretical Analysis. *J. Phys. Chem. B* **2014**, *118*, 14157–14167.
- (40) Wan, X.-K.; Guan, Z.-J.; Wang, Q.-M. Homoleptic Alkynyl-Protected Gold Nanoclusters:  $Au_{44}(PhC\equiv C)_{28}$  and  $Au_{36}(PhC\equiv C)_{24}$ . Angew. Chem., Int. Ed. **2017**, 56, 11494–11497.
- (41) Yang, Z.; Zhimin, L.; Kai, Z.; Gao, L. Controlled Synthesis of  $Au_{36}(SR)_{24}$  (SR = SPh,  $SC_6H_4CH_3$ ,  $SCH(CH_3)Ph$ , and  $SC_{10}H_7$ ) Nanoclusters. *Acta Phys. -Chim. Sin.* **2018**, *34*, 786–791.
- (42) Theivendran, S.; Dass, A. Synthesis of Aromatic Thiolate-Protected Gold Nanomolecules by Core Conversion: The Case of Au<sub>36</sub>(SPh-tBu)<sub>24</sub>. Langmuir **2017**, 33, 7446–7451.
- (43) Rambukwella, M.; Dass, A. Synthesis of Au<sub>38</sub>(SCH<sub>2</sub>CH<sub>2</sub>Ph)<sub>24</sub>, Au<sub>36</sub>(SPh-tBu)<sub>24</sub> and Au<sub>30</sub>(S-tBu)<sub>18</sub> Nanomolecules from a Common Precursor Mixture. *Langmuir* **2017**, *33*, 10958–10964.
- (44) Liao, L.; Zhuang, S.; Wang, P.; Xu, Y.; Yan, N.; Dong, H.; Wang, C.; Zhao, Y.; Xia, N.; Li, J.; et al. Quasi-Dual-Packed-Kerneled Au<sub>49</sub>(2,4-DMBT)<sub>27</sub> Nanoclusters and the Influence of Kernel Packing on the Electrochemical Gap. *Angew. Chem., Int. Ed.* **2017**, *56*, 12644–12648.
- (45) Sumner, L.; Sakthivel, N. A.; Schrock, H.; Artyushkova, K.; Dass, A.; Chakraborty, S. Electrocatalytic Oxygen Reduction Activities of Thiol-Protected Nanomolecules Ranging in Size from Au<sub>28</sub>(SR)<sub>20</sub> to Au<sub>279</sub>(SR)<sub>84</sub>. *J. Phys. Chem. C* **2018**, 122, 24809–24817.

- (46) Dass, A.; Jones, T. C.; Theivendran, S.; Sementa, L.; Fortunelli, A. Core Size Interconversions of  $Au_{30}(S-tBu)_{18}$  and  $Au_{36}(SPhX)_{24}$ . *J. Phys. Chem. C* **2017**, *121*, 14914–14919.
- (47) Theivendran, S.; Chang, L.; Mukherjee, A.; Sementa, L.; Stener, M.; Fortunelli, A.; Dass, A. Principles of Optical Spectroscopy of Aromatic Alloy Nanomolecules: Au<sub>36-x</sub>Ag<sub>x</sub>(SPh-tBu)<sub>24</sub>. J. Phys. Chem. C **2018**, 122, 4524–4531.
- (48) Fan, J.; Song, Y.; Chai, J.; Yang, S.; Chen, T.; Rao, B.; Yu, H.; Zhu, M. The Solely Motif-Doped  $Au_{36-x}Ag_x(SPh-tBu)_{24}$  (x=1-8) Nanoclusters: X-Ray Crystal Structure and Optical Properties. Nanoscale **2016**, 8, 15317–15322.
- (49) Rao, B.; Zhao, T.; Yang, S.; Chai, J.; Pan, Y.; Weng, S.; Yu, H.; Li, X.; Zhu, M. X-Ray Crystal Structure and Doping Mechanism of Bimetallic Nanocluster  $\operatorname{Au}_{36-x}\operatorname{Cu}_x(m\text{-MBT})_{24}$  (x = 1–3). *Dalton Trans* **2018**, 47, 475–480.
- (50) Yang, S.; Chai, J.; Song, Y.; Kang, X.; Sheng, H.; Chong, H.; Zhu, M. A New Crystal Structure of  $Au_{36}$  with a  $Au_{14}$  Kernel Cocapped by Thiolate and Chloride. *J. Am. Chem. Soc.* **2015**, *137*, 10033–10035.
- (51) Schaaff, T. G.; Whetten, R. L. Controlled Etching of Au:SR Cluster Compounds. *J. Phys. Chem. B* 1999, 103, 9394–9396.
- (52) Krause, L.; Herbst-Irmer, R.; Sheldrick, G. M.; Stalke, D. Comparison of Silver and Molybdenum Microfocus X-Ray Sources for Single-Crystal Structure Determination. *J. Appl. Crystallogr.* **2015**, 48, 3–10.
- (53) Sheldrick, G. SHELXT Integrated Space-Group and Crystal-Structure Determination. *Acta Crystallogr., Sect. A: Found. Adv.* **2015**, *A71*, 3–8.
- (54) Sheldrick, G. Crystal Structure Refinement with SHELXL. *Acta Crystallogr., Sect. C: Struct. Chem.* **2015**, *C71*, 3–8.
- (55) Dolomanov, O. V.; Bourhis, L. J.; Gildea, R. J.; Howard, J. A. K.; Puschmann, H. OLEX2: A Complete Structure Solution, Refinement and Analysis Program. *J. Appl. Crystallogr.* **2009**, 42, 339–341.
- (56) Thanthirige, V. D.; Kim, M.; Choi, W.; Kwak, K.; Lee, D.; Ramakrishna, G. Temperature-Dependent Absorption and Ultrafast Exciton Relaxation Dynamics in MAu<sub>24</sub>(SR)<sub>18</sub> Clusters (M = Pt, Hg): Role of the Central Metal Atom. *J. Phys. Chem. C* **2016**, *120*, 23180–23188.
- (57) Müller, P.; Herbst-Irmer, R.; Spek, A.; Schneider, T.; Sawaya, M. Crystal Structure Refinement: A Crystallographer's Guide to SHELXL (IUCr Texts on Crystallography, 8); Oxford University Press: New York. 2006.
- (58) Hutter, J.; Iannuzzi, M.; Schiffmann, F.; VandeVondele, J. CP2K: Atomistic Simulations of Condensed Matter Systems. *Wiley Interdiscip. Rev. Comput. Mol. Sci.* **2014**, *4*, 15–25.
- (59) Goedecker, S.; Teter, M.; Hutter, J. Separable Dual-space Gaussian Pseudopotentials. *Phys. Rev. B: Condens. Matter Mater. Phys.* **1996**, 54, 1703–1710.
- (60) VandeVondele, J.; Hutter, J. Gaussian Basis Sets for Accurate Calculations on Molecular Systems in Gas and Condensed Phases. *J. Chem. Phys.* **2007**, *127*, 114105.
- (61) Grimme, S.; Antony, J.; Ehrlich, S.; Krieg, H. A Consistent and Accurate Ab Initio Parametrization of Density Functional Dispersion Correction (DFT-D) for the 94 Elements H-Pu. *J. Chem. Phys.* **2010**, 132. 154104.
- (62) Perdew, J. P.; Burke, K.; Ernzerhof, M. Generalized Gradient Approximation Made Simple. *Phys. Rev. Lett.* **1996**, *77*, 3865–3868.
- (63) Baseggio, O.; De Vetta, M.; Fronzoni, G.; Toffoli, D.; Stener, M.; Sementa, L.; Fortunelli, A. Time-Dependent Density-Functional Study of the Photoabsorption Spectrum of  $\mathrm{Au}_{25}(\mathrm{SC}_2\mathrm{H}_4\mathrm{C}_6\mathrm{H}_5)_{18}$  Anion: Validation of the Computational Protocol. *Int. J. Quantum Chem.* **2018**, *118*, No. e25769.
- (64) Baseggio, O.; Fronzoni, G.; Stener, M. A New Time Dependent Density Functional Algorithm for Large Systems and Plasmons in Metal Clusters. *J. Chem. Phys.* **2015**, *143*, 024106.
- (65) Baseggio, O.; De Vetta, M.; Fronzoni, G.; Stener, M.; Fortunelli, A. A New Time-Dependent Density-Functional Method for Molecular Plasmonics: Formalism, Implementation, and the

- Au<sub>144</sub>(SH)<sub>60</sub> Case Study. Int. J. Quantum Chem. **2016**, 116, 1603–1611.
- (66) Baerends, E. J.; Ellis, D. E.; Ros, P. Self-consistent Molecular Hartree—Fock—Slater Calculations I. The Computational Procedure. *Chem. Phys.* **1973**, *2*, 41–51.
- (67) van Leeuwen, R.; Baerends, E. J. Exchange-Correlation Potential with Correct Asymptotic Behavior. *Phys. Rev. A: At., Mol., Opt. Phys.* **1994**, 49, 2421–2431.
- (68) Gross, E. K. U.; Kohn, W. Time-Dependent Density-Functional Theory. In *Adv. Quantum Chem.*; Löwdin, P.-O., Ed.; Academic Press: San Diego, CA, 1990; Vol. 21, pp 255–291.
- (69) Baseggio, O.; De Vetta, M.; Fronzoni, G.; Stener, M.; Sementa, L.; Fortunelli, A.; Calzolari, A. Photoabsorption of Icosahedral Noble Metal Clusters: An Efficient TDDFT Approach to Large-Scale Systems. J. Phys. Chem. C 2016, 120, 12773—12782.
- (70) Lenthe, E. v.; Baerends, E. J.; Snijders, J. G. Relativistic Regular Two-Component Hamiltonians. J. Chem. Phys. 1993, 99, 4597–4610.